

Design of the PID temperature controller for an alkaline electrolysis system with time delays

Ruomei Qi^{a,*}, Jiarong Li^{a,*}, Jin Lin^{a,b,**}, Yonghua Song^{a,c}, Jiepeng Wang^{d,e},
Qiangqiang Cui^e, Yiwei Qiu^f, Ming Tang^b, Jian Wang^b

^a*State Key Laboratory of Control and Simulation of Power Systems and Generation Equipment, Department of Electrical Engineering, Tsinghua University, Beijing, China*

^b*Tsinghua-Sichuan Energy Internet Research Institute, Chengdu, China*

^c*Department of Electrical and Computer Engineering, University of Macau, Macau, China*

^d*School of Materials Science and Engineering, Shanghai University, Shanghai, China*

^e*Purification Equipment Research Institute of CSIC, Handan, China*

^f*College of Electrical Engineering, Sichuan University, Chengdu, China*

Abstract

Electrolysis systems use proportional–integral–derivative (PID) temperature controllers to maintain stack temperatures around set points. However, heat transfer delays in electrolysis systems cause manual tuning of PID temperature controllers to be time-consuming, and temperature oscillations often occur. This paper focuses on the design of the PID temperature controller for an alkaline electrolysis system to achieve fast and stable temperature control. A thermal dynamic model of an electrolysis system is established in the frequency-domain for controller designs. Based on this model, the temperature stability is analysed by the root distribution, and the PID parameters are optimized considering both the temperature overshoot and the settling time. The performance of the optimal PID controllers is verified through experiments. Furthermore, the simulation results show that the before-stack temperature should be used as the feedback variable for small lab-scale systems to suppress stack temperature fluctuations, and the after-stack temperature should be used for larger systems to improve the economy. This study is helpful in ensuring the temperature stability and control of electrolysis

*These authors contributed equally.

**Corresponding author

Email address: linjin@tsinghua.edu.cn (Jin Lin)

systems.

Keywords: Electrolysis system, temperature control, PID controller.

Nomenclature

Parameters and variables

\bar{T}	Average temperature
\hat{y}	Control signal for valve opening
ρ	Density
τ	Time delay
A	Area
C	Thermal capacity
c	Specific heat capacity
I	Current
k	Heat transfer coefficient
P	Electricity power
Q	Thermal power
R	Thermal resistance
T	Temperature
t	Time
T_f	Temperature feedback
U	Voltage
u	Control variable, $u = y_{\text{valve}}$
v	Volume flow rate

y_{valve} Valve opening

Superscripts and subscripts

* Steady-state

amb Ambient

c Cooling water

dis Heat dissipation

ele Electrolysis

sep Separator

th Thermal neutral

1. Introduction

Green hydrogen, produced by renewable energy, will play a critical role in the decarbonization of the steel, chemical and transport sectors [1]. As the core element of hydrogen production, it is important to ensure the safe and efficient operation of water electrolysis systems to achieve a steady hydrogen supply. However, the temperature of the electrolysis system is often disturbed by load and ambient temperature fluctuations, which affects both the system efficiency and security. Temperatures lower than the rated temperature will hinder the electrolysis reaction and lead to low efficiencies [3]; on the other hand, high temperatures beyond the upper limit can harm the stack by decreasing the corrosion resistance [4].

In existing commercial electrolysis systems, cooling devices are equipped to maintain the temperature at a set point, and PID temperature controllers are used to suppress the disturbances by regulating the cooling water flow rate [5, 6]. However, heat transfer delays in electrolysis systems make PID tuning to be time-consuming, and the selected PID parameters often fail to achieve satisfactory performance. For example, stack temperature oscillations occur in [7] for both constant and intermittent power inputs caused by the improper PID parameter setting. In [8], the stack temperature does not remain stable under wind power inputs, and the temperature variation is approximately 8 °C with current fluctuations between 40% to 100% rated. Restricted by

temperature variations, the electrolyte temperature is controlled at 65 °C in [8], which is far from the allowable limit of 90 °C; thus, the system efficiency is sacrificed.

For the temperature control of electrolysis systems, systematic modelling and controller design methods are needed. Ulleberg [9] proposed a lumped model to predict the operating temperature of an advanced alkaline electrolyser. This model considers the thermal balance among the heat generation, heat loss and auxiliary cooling, which is widely used in thermal-related studies [10–14]. Y. Qiu presented an optimal production scheduling approach for utility-scale P2H plants considering the dynamic thermal process through a first-order temperature model [15], whose parameters were estimated in [16]. The lumped model does not consider the temperature difference between the stack and the auxiliary devices. Sakas et al. [6] and [17] used second-order and third-order thermal models, respectively, taking into account the thermal inertia of the gas-liquid separators. Time delays exist in heat transfer processes and will affect the accuracy of the model when analysing the temperature of a specific component, e.g., the stack. Qi et al. [18] emphasized the effects of heat transfer delays on the thermal dynamic performance and added two time delay terms for the stack and the cooling coil in the third-order model.

There are few existing studies focusing on temperature control. Sakas et al. [6] used a PID temperature controller in the simulation; however, the dynamic performance of the temperature controller was not discussed. Qi et al. [18] proposed two novel temperature controllers to reduce the temperature overshoot: a current feed-forward PID controller and a model predictive controller. As the most widely used temperature controller in commercial electrolysis systems, the tuning process of the PID temperature controller is a time-consuming task due to the multiple thermal inertia and time delay terms, which have not been discussed yet.

The focus of this paper is on the thermal dynamic analysis and PID controller design of an alkaline electrolysis system. The main contributions are as follows.

1. A frequency-domain thermal model that considers the time delays in the heat transfer process is first proposed for the controller design of electrolysis systems.
2. The temperature stability is analysed by the root distribution, and an optimization model is proposed for parameter tuning considering both

fastness and security, which is verified through experiments.

3. Suggestions are given for system design to improve the thermal dynamic performance. It is suggested to use the before-stack temperature as the feedback variable for small lab-scale systems to suppress the temperature fluctuation and use the after-stack temperature for larger systems to improve the economy. In addition, time delays should be reduced to improve the thermal dynamic performance by increasing the flow rates or using shorter channels.

This paper is organized as follows. In Section II, the complete thermal model of an alkaline electrolysis system, which is linearized and transferred to the frequency domain in Section III is introduced. In Section IV, a method for PID tuning that considers the overshoot and setting time is provided. The proposed PID tuning method is verified through experiments in Section V. In Section VI, the PID temperature controllers are compared with before-stack and after-stack temperature feedbacks. In Section VII, the influence of time delays on the thermal dynamic performance is analysed.

2. Temperature control of an alkaline electrolysis system by the PID temperature controller

2.1. System process description

The process of the analysed alkaline electrolysis system is shown in Fig. 1. The stack is the core element of the system, in which water is electrolyzed to produce hydrogen and oxygen. The gas products mixed with electrolytes enter the gas-liquid separators, in which the gas product is separated for subsequent processing, and the remaining electrolyte from two sides are mixed and circulated into the stack.

The electrolysis reaction in the stack is exothermic at room temperature [9]. To maintain the stack temperature at the rated value, a cooling coil is placed in the gas-liquid separator to cool down the electrolytes and indirectly cool the stack. The cooling water flow rate is controlled by the water valve according to the command from the temperature controller. However, the stack temperature tends to fluctuate considerably in industrial practice due to the inappropriate parameter setting of the temperature controller as well as external disturbances, e.g., current and ambient temperature fluctuations. Thus, it becomes an important issue to obtain stable and fast temperature control.

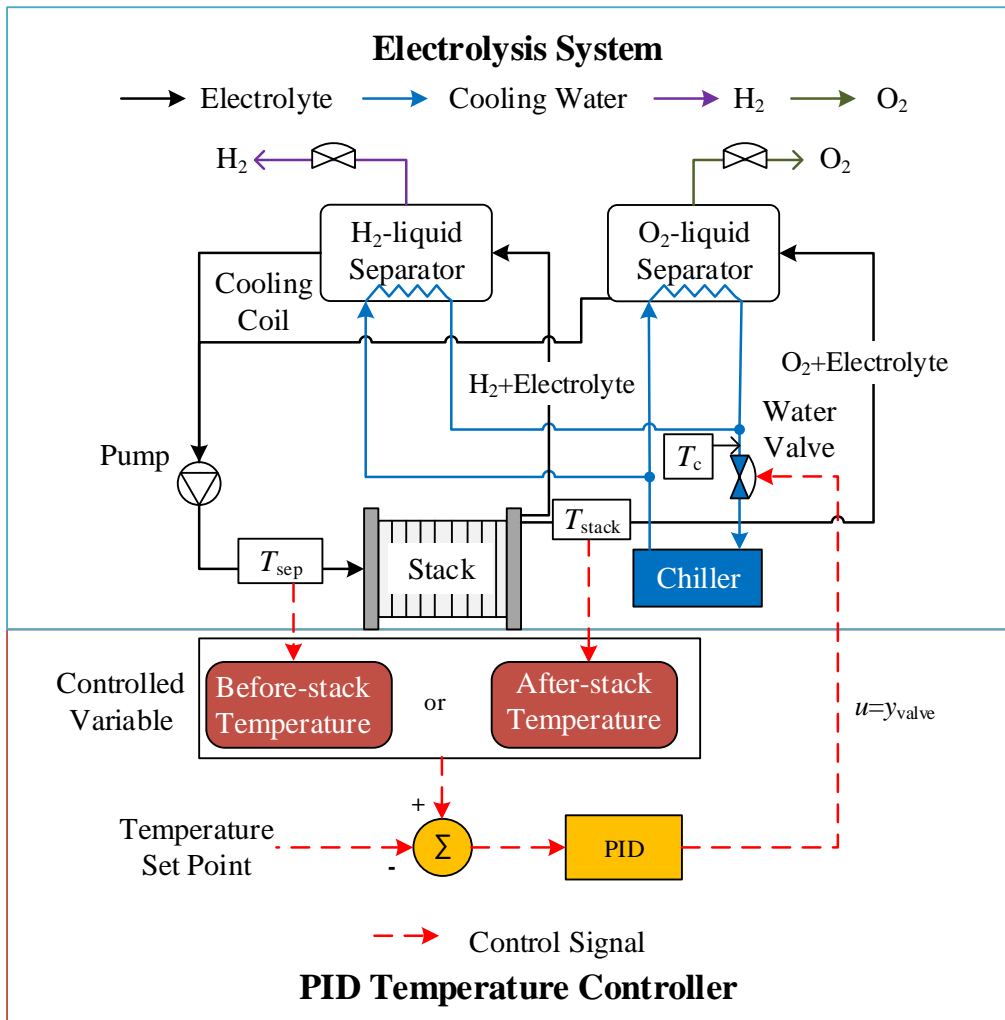


Fig. 1. Thermal management process of an alkaline electrolysis system.

2.2. Thermal dynamic characteristics of the alkaline electrolysis system

The thermal dynamics of the alkaline electrolysis system was modelled as a third-order with time-delays process in our previous article [18]. The state equations are as follows:

$$C_{\text{stack}} \frac{dT_{\text{stack},t}}{dt} = Q_{\text{ele},t} - Q_{\text{dis,stack},t} - c_{\text{lye}} v_{\text{lye}} \rho_{\text{lye}} (T_{\text{stack},t} - T_{\text{sep},t-\tau_1}) \quad (1a)$$

$$C_{\text{sep}} \frac{dT_{\text{sep},t}}{dt} = \frac{1}{2} v_{\text{lye}} \rho_{\text{lye}} c_{\text{lye}} (T_{\text{stack},t} - T_{\text{sep},t}) - kA\Delta T_t - Q_{\text{dis,sep},t} \quad (1b)$$

$$C_c \frac{dT_{c,t}}{dt} = v_{c,t-\tau_2} \rho_c c_c (T_{c,\text{in},t} - T_{c,t}) + kA\Delta T_t \quad (1c)$$

where T_{stack} , T_{sep} and T_c are the temperatures of the stack, gas-liquid separator and cooling coil, respectively, as shown in Fig. 1. Considering that T_{sep} is also the electrolyte temperature at the inlet of the stack, it is referred to as the before-stack temperature in this paper, and T_{stack} is referred to as the after-stack temperature.

In (1), there are two time delay terms τ_1 and τ_2 . τ_1 is the time delay of the stack, which shows that the after-stack temperature T_{stack} changes later than the before-stack temperature T_{sep} by a time-delay τ_1 due to electrolyte convection in the stack. τ_2 is the time delay for the cooling process. When the valve opening command y_{valve} from the controller changes, the influence is delayed by τ_2 to the temperature of the cooling water T_c caused by the slow response of the cooling valve and the electrolyte convection in the cooling coil.

Our experimental results clearly show the existence of the time delays τ_1 and τ_2 , as shown in Fig. 2. The simulation results are in good agreement with the experimental data when $\tau_1 = 6$ min and $\tau_2 = 4$ min are adopted, which are also used in our previous paper [18]. These minute-long delays cause the manual tuning of the PID temperature controller to be very difficult in practice, and oscillations often occur as in Fig. 2.

2.3. PID temperature controller for the electrolysis system

The PID temperature controller is widely used in commercial electrolysis systems [6], as follows (2):

$$y_{\text{valve}} = k_p e_t + k_i \int e_t dt + k_d \frac{de_t}{dt} \quad (2)$$

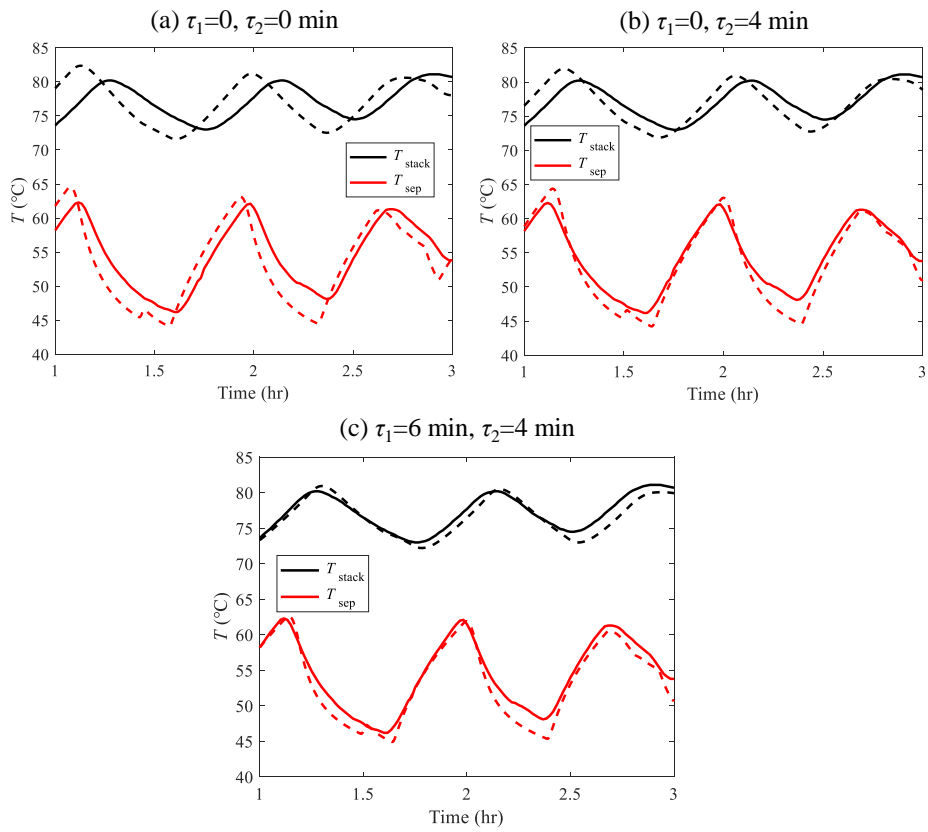


Fig. 2. Comparison of the modelling accuracy with different time delays. The current is fixed at the rated, and the temperature oscillation is caused by improper PID parameter settings. (solid lines: experimental data; dotted lines: simulation results.)

$$e_t = T_{f,t} - T_{\text{aim},t} \quad (3)$$

where k_p , k_i , and k_d are the coefficients for the proportional, integral, and derivative terms, respectively; e_t is the error between the temperature feedback T_f and the set point T_{aim} as (3), and y_{valve} is the valve opening command.

Challenges for PID controller designs lie in both parameter tuning and selecting the feedback variable. The PID parameters k_p , k_i , and k_d have a significant impact on the thermal dynamics of the electrolysis system. In addition, either the inlet temperature T_{sep} or the outlet temperature T_{stack} of the stack can be selected as the feedback variable for the PID temperature controller, as shown in Fig. 1.

This paper answers the following questions.

1. How can the PID parameters be tuned to achieve stable and fast temperature control?
2. How can the temperature feedback for the PID controller be chosen between the before-stack temperature and the after-stack temperature?
3. Will the time delays τ_1 and τ_2 influence the thermal dynamic performance?

3. Frequency-domain model of the alkaline electrolysis system with a PID temperature controller

In this section, the equation set (1)-(3) will be linearized and transformed to the frequency domain for stability analysis and controller design.

3.1. Electrolysis system model

The thermal dynamic model of the electrolysis system (1) can be reorganized as differential-algebraic equations with delays of (4):

$$\begin{cases} \dot{\mathbf{x}} = \mathbf{f}(\mathbf{x}, \mathbf{x}_\tau, \mathbf{y}, \mathbf{y}_\tau, \mathbf{p}, u, u_{\tau_i}) \\ 0 = \mathbf{g}(\mathbf{x}, \mathbf{y}, \mathbf{p}, u) \\ 0 = \mathbf{g}_i(\mathbf{x}_{\tau_i}, \mathbf{y}_{\tau_i}, \mathbf{p}, u_{\tau_i}) \quad i = 1, 2. \end{cases} \quad (4)$$

\mathbf{f} is the state equation vector consisting of the thermal dynamic model for the electrolysis system (1). \mathbf{g} is the algebraic equation vector describing the electrochemical characteristics of the stack and the heat transfer process, as shown in (A.1)-(A.8) in the appendix. \mathbf{x} and \mathbf{y} are the state variable vector and algebraic variable vector, respectively, defined as (5a) and (5b); u is the

control variable as the valve opening y_{valve} ; \mathbf{x}_τ , \mathbf{y}_τ and u_{τ_i} are the variables with time delays defined as (5c)-(5e); and \mathbf{p} is the parameter vector.

$$\mathbf{x} \stackrel{\text{def}}{=} [T_{\text{stack}} \quad T_{\text{sep}} \quad T_c]^T \quad (5a)$$

$$\mathbf{y} \stackrel{\text{def}}{=} [Q_{\text{ele}} \quad Q_{\text{dis,stack}} \quad Q_{\text{dis,sep}} \quad \Delta T_t]^T \quad (5b)$$

$$\mathbf{x}_{\tau_i}(t) = \mathbf{x}(t - \tau_i) \quad i = 1, 2 \quad (5c)$$

$$\mathbf{y}_{\tau_i}(t) = \mathbf{y}(t - \tau_i) \quad i = 1, 2 \quad (5d)$$

$$u_{\tau_i}(t) = u(t - \tau_i) \quad i = 1, 2 \quad (5e)$$

The nonlinear thermal dynamic model (4) can be linearized and transferred to the frequency domain as (6):

$$s\mathbf{x}(s) = \mathbf{A}\mathbf{x}(s) + \mathbf{E}u(s) + \sum_{i=1}^2 (\mathbf{A}_i\mathbf{x}_{\tau_i}(s) + \mathbf{E}_i u_{\tau_i}(s)) \quad (6)$$

where \mathbf{A} , \mathbf{E} , \mathbf{A}_i , and \mathbf{E}_i are the Jacobian matrices, and the details can be found in Appendix B. Then, (6) is reorganized as (7), and the transfer function of the electrolysis system G_p is derived as (8):

$$\mathbf{x}(s) = \frac{\mathbf{E} + \sum_{i=1}^2 \mathbf{E}_i e^{-\tau_i s}}{s\mathbf{I} - \mathbf{A} - \sum_{i=1}^2 \mathbf{A}_i e^{-\tau_i s}} u(s) \quad (7)$$

$$G_p(s) = \frac{T_f(s)}{u(s)} = \frac{\mathbf{F}\mathbf{x}(s)}{u(s)} = \frac{\mathbf{F}(\mathbf{E} + \sum_{i=1}^2 \mathbf{E}_i e^{-\tau_i s})}{s\mathbf{I} - \mathbf{A} - \sum_{i=1}^2 \mathbf{A}_i e^{-\tau_i s}} \quad (8)$$

where \mathbf{F} shows the selection of the temperature feedback T_f :

$$\mathbf{F} = \begin{cases} \begin{pmatrix} 1 & 0 & 0 \end{pmatrix}, & \text{if } T_f = T_{\text{stack}}, \\ \begin{pmatrix} 0 & 1 & 0 \end{pmatrix}, & \text{if } T_f = T_{\text{sep}}. \end{cases} \quad (9)$$

3.2. System model with a PID temperature controller

The PID temperature controller equations (2)-(3) can also be transferred into the frequency domain:

$$u(s) = G_c(s)e(s) = G_c(s)(T_f(s) - T_{\text{aim}}(s)) \quad (10a)$$

$$G_c(s) = k_p + k_i/s + k_d s \quad (10b)$$

Combining (7) and (10), the closed-loop transfer function of the system is:

$$G(s) = \frac{T_f(s)}{T_{\text{aim}}(s)} = \frac{-G_c(s)G_p(s)}{1 - G_c(s)G_p(s)}. \quad (11)$$

The poles λ of the closed-loop transfer function (11) determine the characteristic of the thermal dynamic process, which can be calculated by the characteristic equation as (12). The transcendental terms $e^{-\tau s}$ can be replaced by the Padé approximation, and a first-order form is (13).

$$1 - G_c(\lambda)G_p(\lambda) = 0. \quad (12)$$

$$e^{-\tau s} \approx \frac{-\tau s/2 + 1}{\tau s/2 + 1} \quad (13)$$

A block diagram can be derived from the linear model (6) as Fig. 3 to show the thermal dynamic process more intuitively. Fig. 3 gives a clear physical meaning to each Jacobian element in matrices \mathbf{A} , \mathbf{E} , \mathbf{A}_i , and \mathbf{E}_i . The diagonal elements indicate the thermal inertia of the devices. Moreover, $\mathbf{A}(1, 1)$, $\mathbf{A}(2, 2)$, and $\mathbf{A}(3, 3)$ represent the time constant (the inverse of thermal inertia) of the stack, the gas-liquid separator and the cooling coil, respectively; while the nondiagonal elements are the gain coefficients. Furthermore, Fig. 3 compares PID temperature controllers with different temperature feedback variables T_f , shown by dotted lines. When the after-stack temperature T_{stack} is adopted as the feedback variable T_f , the thermal inertia of the stack, controller and separator are connected in series so that the total thermal inertia of the system increases. On the other hand, when the before-stack temperature T_{sep} is used as the feedback, the thermal inertia of the stack is in parallel with the other auxiliaries, and the system inertia is reduced, leading to better dynamic performance. The simulation results are shown in Section 6.

3.3. The thermal dynamic characteristics

The closed-loop transfer function $G(s)$ (11) is of high-order with $n_\lambda = 6$ poles and $n_\nu = 4$ zeros, in which two pole-zero pairs are introduced by the time delays τ , three poles by the thermal inertia C and others by the PID controller. Fig. 4 shows a root-locus plot, which draws the zero and pole distributions with changing PID parameters. The parameters used for the electrolysis system model (1) are from a $5 \text{ Nm}^3/\text{hr}$ alkaline electrolysis

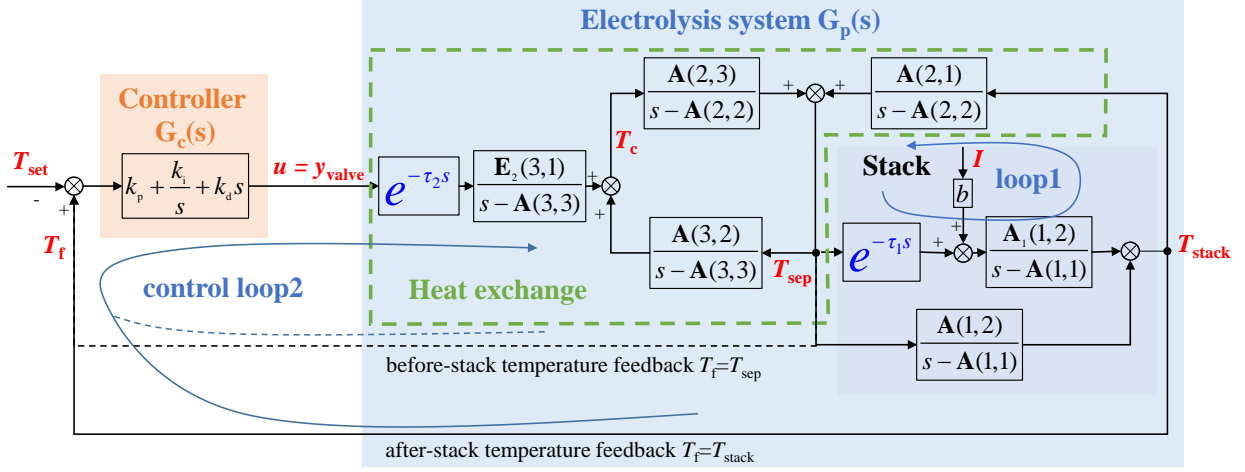


Fig. 3. The structure block of the alkaline electrolysis system.

platform CNDQ5 [18] and summarized in Appendix C. In Fig. 4, only the zeros and poles within 10 times the real part of the dominant pole are shown, and those far from the imaginary axis are ignored because their influences on the system dynamics are weak. The real parts of the roots are close to each other, and different poles may become the dominant pole determining the system dynamics when the PID parameters change. Therefore, there is no fixed dominant pole for the thermal dynamic process, and it is difficult to approximate it as a second-order system.

This high-order characteristic makes it difficult to use the time response-based PID tuning method, which selects the suitable pole and zero positions of a controller. Instead, we simply use an optimization model to select the optimal PID parameters considering both the temperature overshoot γ and setting time t_s in the next section.

4. Parameter tuning of the PID temperature controller

In this section, a tuning method for the PID temperature controller is provided. The stability region is derived based on the linearized frequency-domain model (11). The optimal PID parameters are selected by maximizing the temperature overshoot and the setting time in the stability region.

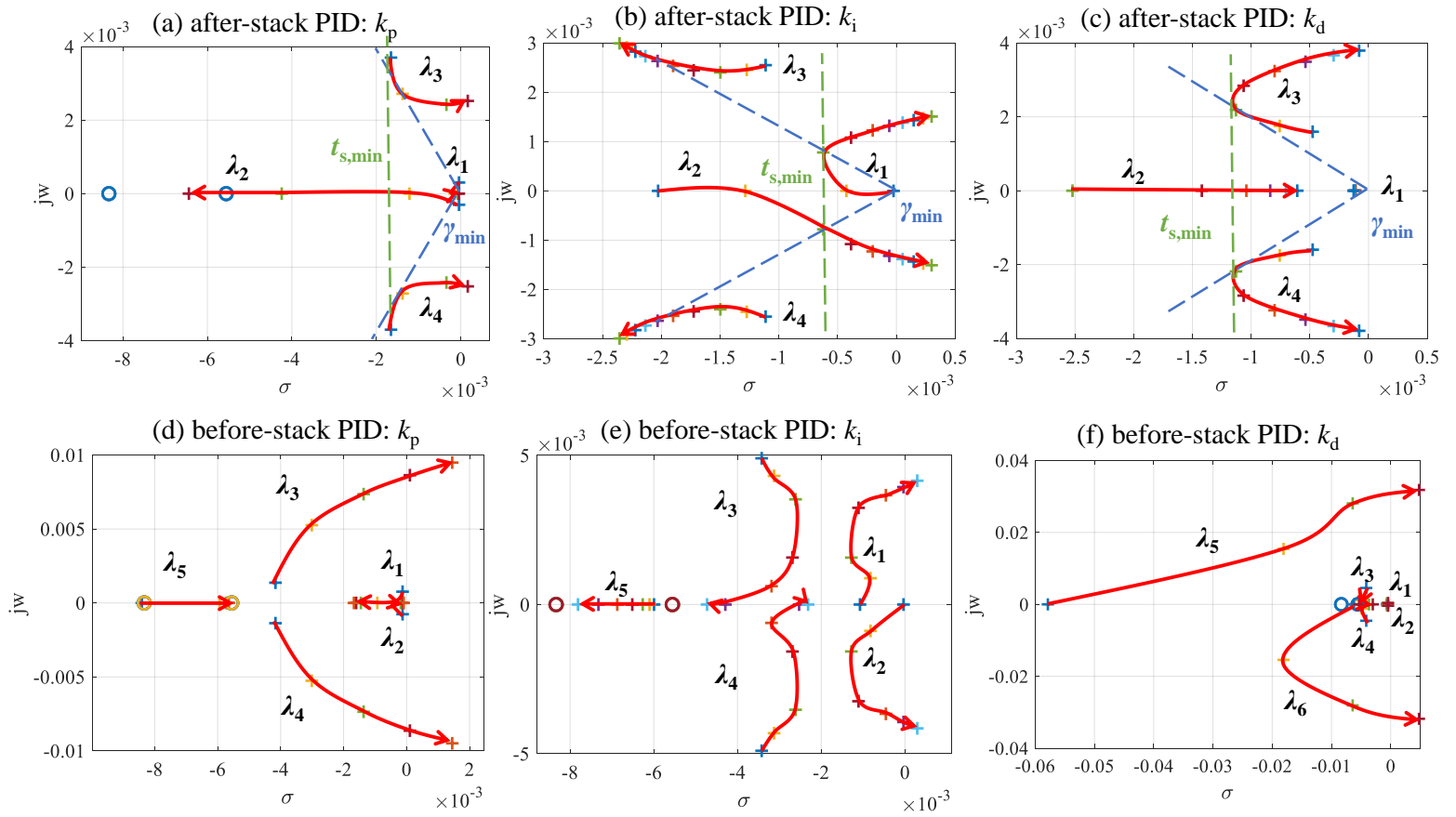


Fig. 4. The root-locus plots with varying PID parameters (+: poles, o: zeros).

4.1. Stability analysis

The stack temperature should be asymptotically stable, which means that an equilibrium temperature is eventually reached after the disturbance. The stability can be judged by the stability criteria: a transfer function is stable if all its poles have a negative real part [19]. Therefore, the system temperature is stable if:

$$\lambda_i = \sigma_i + jw_i, i = 1, 2, \dots, n_\lambda \quad (14)$$

$$\sigma_i < 0, i = 1, \dots, n_\lambda. \quad (15)$$

where σ_i and jw_i are the real and imaginary parts of the i th pole λ_i , respectively, derived from (12). The PID parameters (k_p, k_i, k_d) satisfying (15) form the stability region.

4.2. PID tuning by optimization

On the premise of temperature control stability, the dynamic performance becomes important, and we pay special attention to the security and fastness of the temperature controller. The temperature overshoot γ and the settling time t_s are selected as the performance indicators defined as follows:

1. Temperature overshoot γ evaluates the maximum variation of the controlled temperature from the set point T_{set} after a disturbance:

$$\gamma = (T_{\text{peak}} - T_\infty)/T_\infty \quad (16)$$

where T_{peak} is the peak temperature and T_∞ is the steady-state value. γ is usually defined as (16) under the step response process and zero initial condition in control theory [19]. A large temperature overshoot γ will cause the stack temperature to exceed the permissible limit and cause safety problems.

2. The setting time t_s is the time required to reach and remain within $\pm 2\%$ of the steady state value T_∞ for a step response process. A long setting time t_s will cause temperature error accumulation since the stack temperature has not returned to the set point T_{set} when the load changes again.

The optimal PID parameters can be derived by (17):

$$\min_{k_p, k_i, k_d} (\gamma/\gamma_0)^2 + (t_s/t_{s,0})^2 \quad (17)$$

where γ_0 and $t_{s,0}$ are the reference overshoot and setting time, respectively, used to unify the order of magnitude of the two parts. The optimization problem (17) can be solved by traversing the PID parameters in the stability region, and the overshoot γ and setting time t_s are calculated by applying a unit step change on the temperature set point T_{aim} based on the closed-loop transfer function $G(s)$ as (11).

In addition to the optimization method above, the PID parameters can also be obtained by using commercial PID parameter tuning software (e.g., MATLAB PID tuner) with the closed-loop transfer function $G(s)$ as (11). The advantage of the optimization method (17) is that the reference values γ_0 and $t_{s,0}$ can be easily adjusted based on the permitted temperature overshoot and setting time. In addition, an optimal PID parameter exists for the after-stack PID temperature controller at the intersection of the minimum overshoot line γ_{min} and the minimum setting time line $t_{s,\text{min}}$ shown in the root-locus plot Fig. 4, which can be found by the optimization problem (17).

5. PID temperature controller design and verification for a 5 Nm³/hr alkaline electrolysis platform

The proposed PID tuning method is verified on a commercial 5 Nm³/hr alkaline electrolysis platform CNDQ5 from the Purification Equipment Research Institute of CSIC. The details of this system can be found in our previous article [18]. The values of the parameters in the thermal dynamic model (1) are summarized in Appendix C.

5.1. Optimal PID parameters

The stability regions of the after-stack and before-stack temperature controllers are shown in Fig. 5, which are derived by linearizing the thermal dynamic model (4) at the equilibrium point with a rated current $I = 820$ A and after-stack temperature $T_{\text{stack}} = 80^\circ\text{C}$. The allowed PID parameters are within the region formed by the curves and the coordinate axes. If any PID parameter is on or outside the boundary, the stack temperature T_{stack} will oscillate or overheat. Comparing the two kinds of controllers in Fig. 5, it can be seen that the stability region of the after-stack temperature controller is much smaller than that of the before-stack temperature controller, which is why manual tuning of the after-stack temperature controller is more difficult. In addition, the after-stack temperature controller allows a larger derivative

term k_d to predict the temperature change and offset the influence of thermal inertia and time delays. The before-stack temperature controller has a smaller upper limit for the differential term k_d , which indicates that a PI controller may be able to reduce the parameter tuning difficulty.

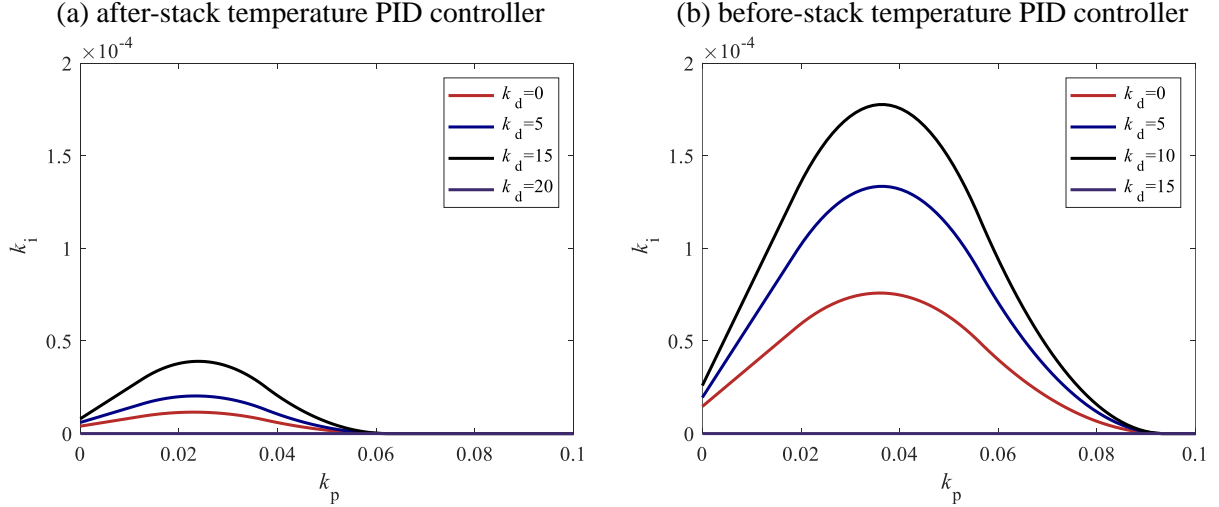


Fig. 5. The stability regions of the after-stack and before-stack PID temperature controllers.

The PID parameters are derived by solving the optimization problem (17). The reference overshoot γ_0 and setting time t_s are selected as 50% and 2 hr, respectively. A regular grid of $10 \times 10 \times 10$ sampling points of control parameters (k_p, k_i, k_d) is employed in the traversing process. The optimal PID parameters are shown in Table 1.

Table 1: Optimal parameters derived through optimization (17)

Type	k_p	k_i	k_d
After-stack feedback	0.02	1.1×10^{-5}	6
Before-stack feedback	0.031	3.1×10^{-5}	0

5.2. Experimental results

The optimal PID temperature controllers in Table 1 are applied to the CNDQ5 platform to maintain the controlled temperature (T_{stack} or T_{sep}) around the set point T_{aim} under current disturbance. The temperature set

point T_{aim} of the after-stack PID controller is set to 70°C and the before-stack PID controller to 50°C. The sampling time of the PID controller is 1 s. The experimental results are shown in Fig. 6.

It is clear that both PID controllers can achieve stable temperature control and that the controlled temperature (T_{stack} or T_{sep}) gradually approaches the set point T_{aim} . The oscillation that occurred in Fig. 6(b) is caused by the fluctuation of the cooling water inlet temperature $T_{\text{c,in}}$ as a result of the improper PID parameter setting of the chiller. By using a fixed cooling water temperature $T_{\text{c,in}} = 30^\circ\text{C}$ in the simulation, the oscillation is eliminated, as shown by the dotted lines in Fig. 6(b). In the experiment, the temperature set point T_{aim} is fixed at 70°C and 50°C for the after-stack PID controller and the before-stack PID controller, respectively. However, in Fig. 6(a), the after-stack temperature T_{stack} is lower than the set point $T_{\text{aim}} = 70^\circ\text{C}$ during 0-0.5 hr, which is caused by the large heat dissipation to the ambient Q_{dis} . The experiments are carried out in winter when the ambient temperature T_{amb} is approximately 0 to 10°C. This low temperature makes it difficult to carry out experiments. The start-up process takes approximately 4 to 5 hours. In addition, the load interval that requires cooling is very narrow, which is not conducive to testing the temperature controller.

The simulation results of the time-domain model (4) are shown in Fig. 6 by the dotted lines. The thermal dynamic model shows very high accuracy compared to the experimental data. The difference is mainly caused by the hysteretic characteristic of the cooling water valve, which is ignored in the modelling [18]. The high accuracy of the thermal dynamic model allows for the comparison of different PID designs and analyse the effect of time delays by simulation in the following sections.

6. Comparison between the after-stack and before-stack PID temperature controllers

In this section, the PID temperature controllers are compared with different feedbacks: the after-stack PID temperature controller and the before-stack PID temperature controller, shown in Fig. 1. To obtain results with better flexibility, we use the nonlinear model (4) in the simulation, and the ambient temperature T_{amb} is set to 25°C. In addition, the optimal PID parameters in Table 1 are adopted.

Fig. 7 shows the thermal dynamic performance of the electrolysis system under the temperature set point regulation and current disturbance scenarios.

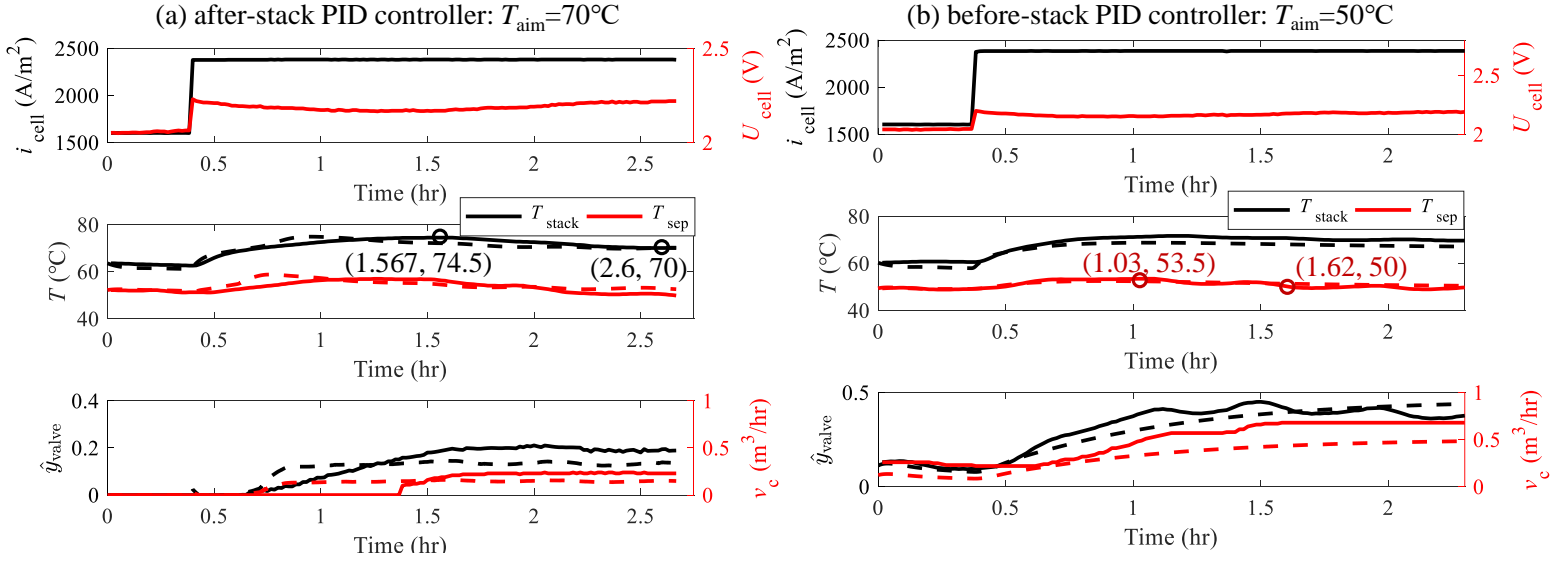


Fig. 6. Experimental results for the optimal PID temperature controllers under a step current. (solid lines: experimental data; dotted lines: simulation results.)

In Fig. 7(a), it is clear that the before-stack PID temperature controller can approach the set point T_{aim} faster than the after-stack PID temperature controller. This is because the thermal inertia is reduced with a before-stack temperature feedback, as illustrated in the structure block Fig. 3. During 4.5-5.5 hr, the after-stack temperature T_{stack} of the system with an after-stack PID temperature controller has not reached the temperature set point $T_{\text{aim}} = 70^\circ\text{C}$ and is still in a slow heat-up process, since the integration term k_i is very small at approximately 1.1×10^{-5} in Table 1.

In Fig. 7(b), the before-stack PID temperature controller also shows better resistance to current disturbances compared to the after-stack PID temperature controller. It requires a shorter time to return to the temperature set point T_{aim} , and the maximum temperature deviation ΔT_{max} is smaller: the before-stack PID temperature controller has $\Delta T_{\text{max}} = 2^\circ\text{C}$, and the after-stack PID temperature controller has $\Delta T_{\text{max}} = 5.88^\circ\text{C}$. This advantage can be explained by the structure block as Fig. 3: for the before-stack PID controller, the thermal inertia $\mathbf{A}(1, 2)/(s - \mathbf{A}(1, 1))$ of the stack and the heat transfer delay τ_1 are not in the control loop 2; thus, the valve opening y_{valve} is closer to the temperature feedback T_{sep} , resulting in a more timely adjustment of the cooling valve.

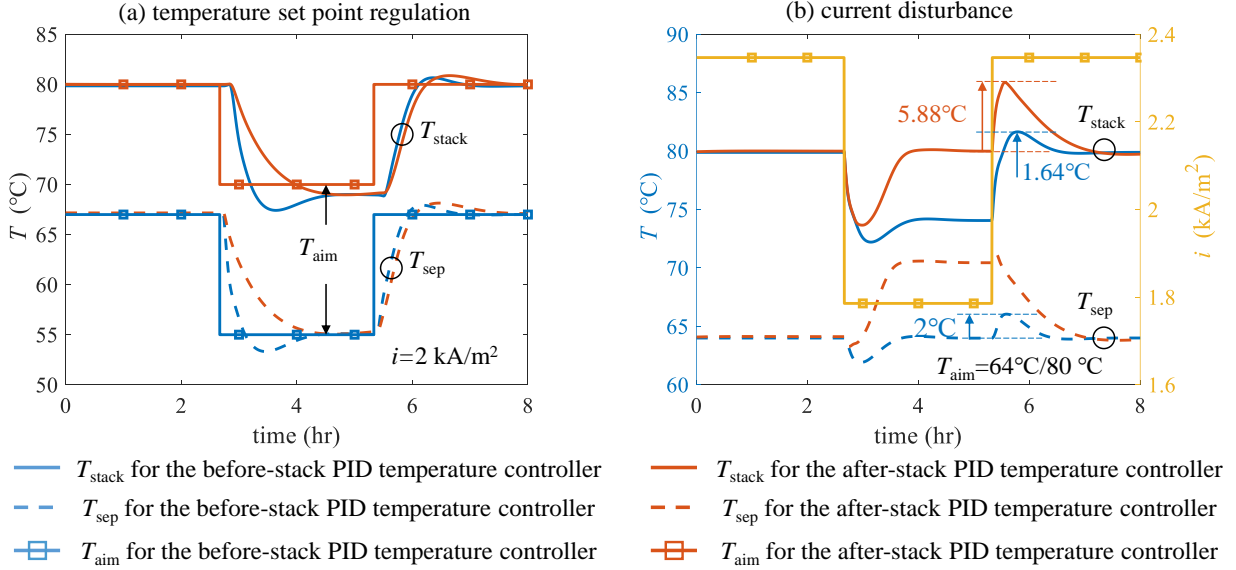


Fig. 7. Comparison of the after-stack and before-stack PID temperature controllers under (a) temperature set point regulation and (b) current disturbance scenarios.

The resistance to current disturbances is significant for electrolysis systems under dynamic operation, e.g., in renewable-to-hydrogen scenarios. The thermal dynamic performance of the two PID temperature controllers are compared in Fig. 8 with the wind power input from a wind turbine generator that is averaged and received every 1 hr [20]. Statistics indicating the temperature control performance are shown in Table 2.

From Table 2, the before-stack PID temperature controller has better dynamic performance considering the maximum temperature deviation ΔT_{max} and the fluctuation of the controlled temperature δ_T . For the after-stack PID temperature controller, the stack temperature T_{stack} exceeds the set point T_{aim} with a deviation of $\Delta T_{\text{max}} = 5.26^\circ\text{C}$ when the current suddenly increases at $t = 16$ hr. This temperature deviation ΔT_{max} makes it necessary for the after-stack PID temperature controller to leave a certain margin between the temperature set point T_{aim} and the upper limit; otherwise, the stack will be overheated and cause safety problems. Furthermore, the controlled temperature fluctuation of the after-stack PID temperature controller in the medium load region is larger than that of the before-stack PID temperature controller, as shown in δ_T in Table 2. This can also be observed in Fig. 8 since the before-stack temperature T_{sep} of the before-stack PID

temperature controller is stable in the full operating intervals.

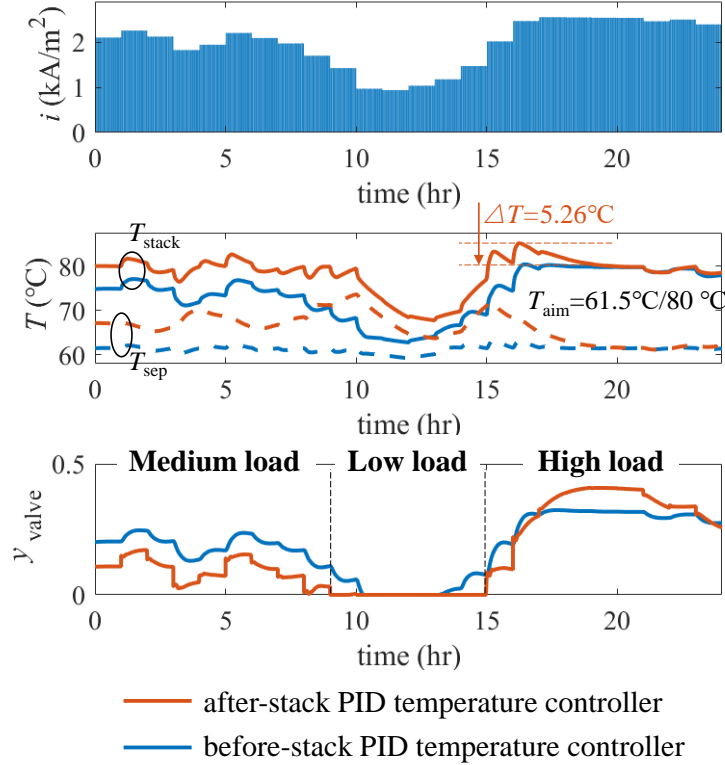


Fig. 8. Comparison of the after-stack and before-stack PID temperature controllers under the peak shaving scenario.

Although the before-stack PID temperature controller has the advantages described above, it is not always the best choice. The average stack temperature \bar{T} is reduced during low and medium loading periods since the before-stack temperature T_{sep} is fixed at T_{set} , leading to an efficiency loss. On the other hand, the after-stack PID temperature controller can achieve a high average electrolysis temperature \bar{T} and ensure safe operation since the hottest spot in the stack is always at the outlet T_{stack} .

Table 3 gives suggestions on the temperature feedback selection. For small lab-scale systems, it is preferred to use the before-stack temperature T_{sep} as the feedback because the thermal capacity C of the system is small and the stack temperature tends to fluctuate considerably under disturbances, e.g., current and ambient temperature. In addition, the after-stack PID tempera-

Table 2: Comparison of the thermal dynamic performance in peak shaving scenario

	Before-stack PID	After-stack PID
Maximum temperature deviation from the set point ΔT_{\max}	1.82°C	5.26°C
Controlled temperature variance during medium loading δ_T^*	0.46°C	1.31°C
Average stack temperature \bar{T}^{**}	67.58°C	72.27°C

$$* \delta_T = \sqrt{\sum_{i=1}^N (T_i - T_{\text{aim},i})^2 / N}, T = T_{\text{sep}} \text{ or } T_{\text{stack}}$$

$$** \bar{T} = \sum_{i=1}^N (T_{\text{sep},i} + T_{\text{stack},i}) / (2N)$$

ture controller is more suitable for larger commercial systems to improve the economy.

Table 3: PID controller comparison

Controller	Advantages	Disadvantages
Before-stack PID	Less fluctuation under dynamic operation	Low average temperature during low-load periods
After-stack PID	High efficiency	More fluctuation under dynamic operation

7. Effect of the time delays on the thermal dynamic performance

The impact of the time delays τ_1 and τ_2 on the thermal dynamic performance is analysed in this section to optimize the performance in the system design process.

The stability regions with different time delays for the after-stack PID temperature controller are shown in Fig. 9. When the time delay τ_1 or τ_2 increases, the stability region decreases monotonically. This indicates that for the after-stack PID temperature controller with large time delays, the allowed PID parameter domain is extremely narrow, which causes PID tuning to be difficult.

For the before-stack PID temperature controller, the influence of the time delay of the stack τ_1 on the stability region is different from that of the after-stack PID controller, as shown in Fig. 10(a). When the derivative term $k_d = 0$, the stability region increases slightly and then remains almost the

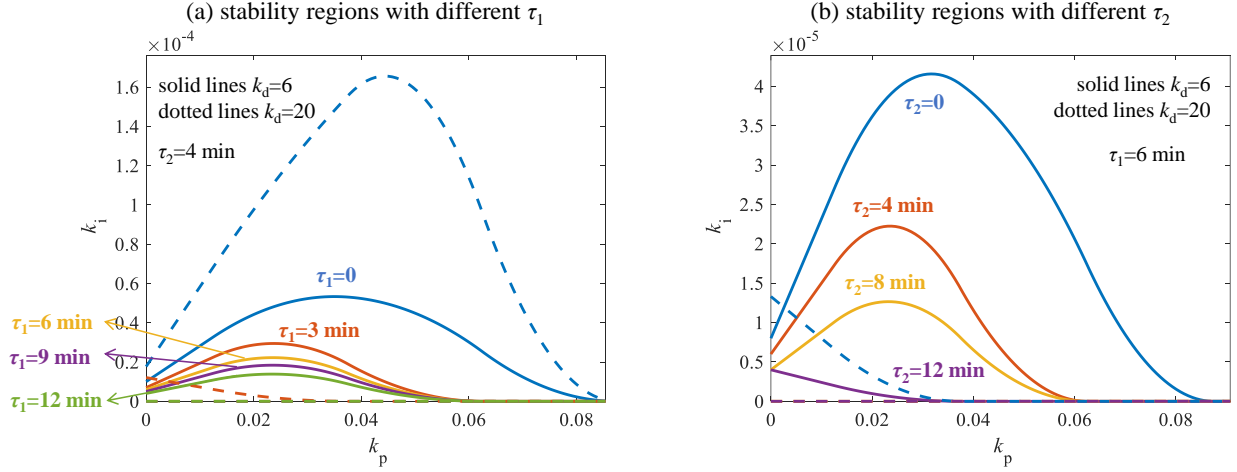


Fig. 9. Stability region of the after-stack PID controller at different time-delays.

same with the increasing time delay of the stack τ_1 . This is attributed to the position of τ_1 , as shown in the structure block Fig. 3. The time delay of the stack τ_1 is in the positive feedback loop 1, which can be beneficial to the system stability for some PID parameter settings. For example, when the before-stack temperature T_{sep} increases due to disturbances, τ_1 delays the further increase of T_{sep} through loop 1. On the other hand, the time delay of the cooling process τ_2 is inside the control loop 2, which is a negative feedback loop and therefore worsens the stability, as shown in Fig. 10(b).

The relationships between the time delays and the thermal dynamic performance of the system are analysed using performance indicators, that is, the temperature overshoot γ and the settling time t_s , shown as Fig. 11. The blue dots show the performances of the optimal PID controllers at the different time delays τ_1 and τ_2 . A surface as (18) is used to show the changing trend, in which a_1 - a_4 are the fitting parameters.

$$\tau/t_s = a_1 + a_2\tau_1 + a_3\tau_2 + a_4\tau_1\tau_2 \quad (18)$$

From Fig. 11, it is clear that smaller time delays $\tau_1\tau_2$ lead to faster response t_s and reduced overshoot γ , which is beneficial to effective temperature control. Compared with the no-delay circumstance, $\tau_1 = \tau_2 = 12$ min will increase the setting time t_s from 0.17 hr to 3.69 hr and the overshoot γ from 0% to 25.94% for the after-stack PID controller. A similar phenomenon is also observed for the before-stack PID controller: $\tau_1 = \tau_2 = 12$ min increases

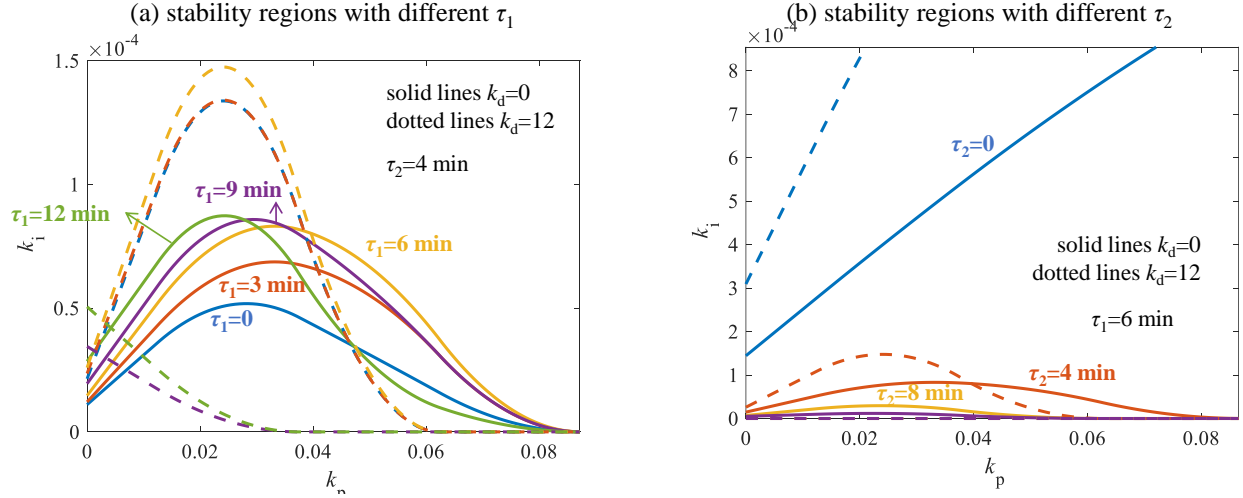


Fig. 10. Stability region of the before-stack PID controller at different time-delays.

the setting time t_s from 0.197 hr to 0.96 hr, while the overshoot γ remains 2% below. Furthermore, from the slope of the surface, it can be seen that the before-stack PID temperature controller is less sensitive to the time delay variation and can tolerate large time delays. For the before-stack PID temperature controller, τ_2 has a greater impact on the performance compared to τ_1 , which is consistent with the results obtained from the stability analysis in Fig. 10.

Time delays should be reduced during the system design to avoid slow temperature regulations and large overshoots. The time delay of the stack τ_1 is caused by the electrolyte convection in the stack and can be reduced by increasing the electrolyte flow rate or using shorter channels. The time delay of the cooling process τ_2 represents the time from the change in the valve opening command y_{valve} to the change in the outlet temperature of the cooling coil T_c , which can be reduced by adopting a larger cooling water flow rate v_c or optimizing the structure of the cooler (shorter cooling pipelines). In addition, moving the cooler closer to the stack, rather than putting the cooling coil in the gas-liquid separator as Fig. 1, is also beneficial to improve the thermal performance because the cooling effect can be applied on the stack as soon as possible.

In recent years, large-scale alkaline electrolysis systems have become a development trend, and the long pipelines between modules make the time-delays obvious. In such scenarios, evaluating and eliminating the influence of

time delays become significant to improve the dynamic performance of the system.

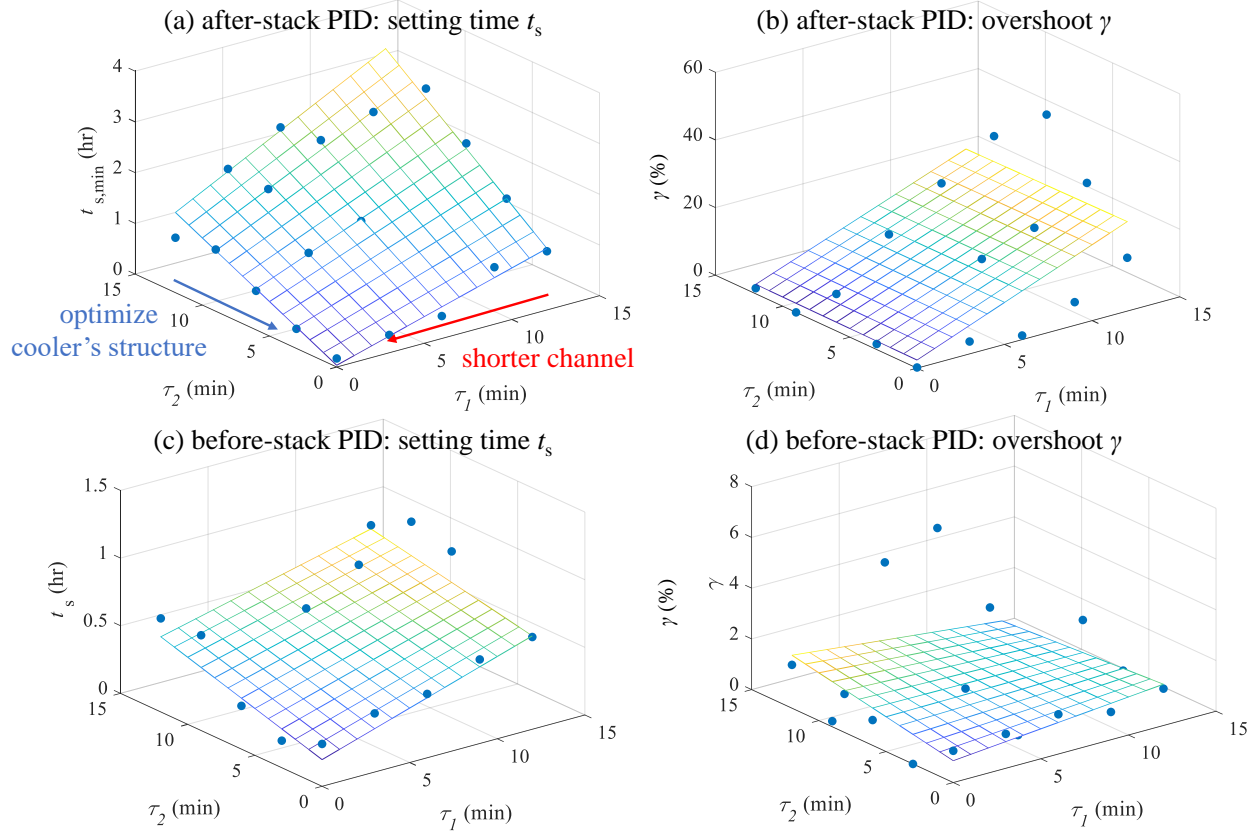


Fig. 11. Setting time t_s and overshoot γ at different time-delays. (a)(b) After-stack PID temperature controller. (c)(d) Before-stack PID temperature controller.

8. Conclusion

This study shows how to design a PID temperature controller in an alkaline electrolysis system with time delays. A frequency-domain model (11) that can be directly used for PID tuning is derived. In addition, an optimization-based PID tuning method is proposed to minimize both the temperature setting time t_s and overshoot γ .

The effectiveness of the proposed PID tuning method is verified through experiments. Furthermore, a detailed comparison between the after-stack

and the before-stack PID temperature controllers is carried out through simulation. The results show that the before-stack PID temperature controller has better thermal dynamic performance than the after-stack PID temperature controller, although the system efficiency is sacrificed at low-loading periods. It is suggested to use the before-stack temperature T_{sep} as the feedback variable for small lab-scale systems to suppress the stack temperature fluctuation and use the after-stack temperature T_{stack} for larger systems to improve the economy.

The influence of time delays on the thermal dynamic performance is also discussed. Larger time delays result in a longer setting time t_s and larger overshoot γ . Optimization methods should be considered in the design process, including increasing the electrolyte and cooling water flow rate, optimizing the structure of the cooler, and moving the cooler closer to the stack.

This study is helpful for the temperature controller design of electrolysis systems. Although the alkaline electrolysis system is the focus in this study, the method given is suitable for both alkaline and proton exchange membrane (PEM) electrolysis systems and for different system structures.

Appendix A. Algebraic equations in the thermal dynamic model

The heat produced $Q_{\text{ele},t}$ is proportional to the electrolysis current I_{cell} as (A.1):

$$Q_{\text{ele}} = (U_{\text{cell}} - U_{\text{th}})I_{\text{cell}}N_{\text{cell}} \quad (\text{A.1})$$

and an empirical relationship is used for calculating the cell voltage U_{cell} :

$$U_{\text{cell},t} = U_{\text{rev}} + (r_1 + r_2\bar{T}_t)i_t + s \log((t_1 + t_2/\bar{T}_t + t_3/\bar{T}_t^2)i_t + 1) \quad (\text{A.2})$$

$$\bar{T}_t = (T_{\text{stack},t} + T_{\text{sep},t})/2. \quad (\text{A.3})$$

The heat loss to the ambient $Q_{\text{dis,stack}}$ is composed of the thermal convection term Q_{conv} and the radiation term Q_{rad} :

$$Q_{\text{dis,stack}} = Q_{\text{conv}} + Q_{\text{rad}} = hA_{\text{stack}}(T_{\text{stack}} - T_{\text{amb}}) + \sigma A_{\text{stack}}\varepsilon_{\text{stack}}(T_{\text{stack}}^4 - T_{\text{amb}}^4) \quad (\text{A.4})$$

$$h = 2.51 \times 0.52 \left(\frac{(T_{\text{stack}} - T_{\text{amb}})}{\varphi_{\text{stack}}} \right)^{0.25}. \quad (\text{A.5})$$

The time-delay term τ_1 in (1a) represents the delay from the change in the before-stack temperature T_{sep} to the change in the after-stack temperature T_{stack} .

(1b) and (1c) illustrate the heat exchange process from the electrolyte in the separator to the cooling water. T_{sep} is the outlet temperature of the separator, which is also the before-stack temperature, as shown in Fig. 1, and T_c is the outlet temperature of the cooling coil. The mean logarithmic temperature difference ΔT_t and the heat dissipation to the ambient $Q_{\text{dis,sep}}$ are:

$$\Delta T_t = \frac{(T_{\text{stack},t} - T_{c,t}) - (T_{\text{sep},t} - T_{c,\text{in},t})}{\ln((T_{\text{stack},t} - T_{c,t}) / (T_{\text{sep},t} - T_{c,\text{in},t}))} \quad (\text{A.6})$$

$$Q_{\text{dis,sep}} = \frac{\bar{T} - T_{\text{amb}}}{R_{\text{sep}}}. \quad (\text{A.7})$$

The cooling water flow rate $v_{c,t}$ in (1c) is proportional to the valve opening $y_{\text{valve},t}$ as (A.8), and a time-delay term τ_2 is introduced to show the delay from the change of cooling water flow rate v_c to the cooling coil's temperature T_c .

$$v_{c,t} = k_{\text{valve}} y_{\text{valve},t}. \quad (\text{A.8})$$

Appendix B. Methods for model linearization and transformation to frequency domain

Discretizing the nonlinear model (4) at an equilibrium point $(\mathbf{x}^*, \mathbf{y}^*, u^*)$:

$$\begin{cases} \Delta \dot{\mathbf{x}} = \tilde{\mathbf{A}} \Delta \mathbf{x} + \tilde{\mathbf{B}} \Delta \mathbf{y} + \sum_{i=1}^2 \left(\tilde{\mathbf{A}}_i \Delta \mathbf{x}_{\tau_i} + \tilde{\mathbf{B}}_i \Delta \mathbf{y}_{\tau_i} \right) \\ 0 = \tilde{\mathbf{C}} \Delta \mathbf{x} + \tilde{\mathbf{D}} \Delta \mathbf{y} + \tilde{\mathbf{E}} \Delta u \\ 0 = \tilde{\mathbf{C}}_i \Delta \mathbf{x}_{\tau_i} + \tilde{\mathbf{D}}_i \Delta \mathbf{y}_{\tau_i} + \tilde{\mathbf{E}}_i \Delta u_{\tau_i}, \quad i = 1, 2 \end{cases} \quad (\text{B.1})$$

where $\Delta \mathbf{x} = \mathbf{x} - \mathbf{x}^*$ and $\Delta \mathbf{y} = \mathbf{y} - \mathbf{y}^*$, and the Jacobian matrices are as follows:

$$\tilde{\mathbf{A}} = J(\mathbf{f}, \mathbf{x}) \quad \tilde{\mathbf{B}} = J(\mathbf{f}, \mathbf{y}) \quad \tilde{\mathbf{C}} = J(\mathbf{g}, \mathbf{x}) \quad \tilde{\mathbf{D}} = J(\mathbf{g}, \mathbf{y}) \quad \tilde{\mathbf{E}} = J(\mathbf{g}, \mathbf{u}) \quad (\text{B.2})$$

$$\tilde{\mathbf{A}}_i = J(\mathbf{f}, \mathbf{x}_{\tau_i}) \quad \tilde{\mathbf{B}}_i = J(\mathbf{f}, \mathbf{y}_{\tau_i}) \quad \tilde{\mathbf{C}}_i = J(\mathbf{g}_i, \mathbf{x}_{\tau_i}) \quad \tilde{\mathbf{D}}_i = J(\mathbf{g}_i, \mathbf{y}_{\tau_i}) \quad \tilde{\mathbf{E}}_i = J(\mathbf{g}_i, \mathbf{u}_{\tau_i}) \quad (\text{B.3})$$

$$J(\mathbf{f}, \mathbf{x}) = \left[\begin{array}{ccc} \frac{\partial f_1}{\partial x_1} & \dots & \frac{\partial f_1}{\partial x_n} \\ \vdots & \ddots & \vdots \\ \frac{\partial f_n}{\partial x_1} & \dots & \frac{\partial f_n}{\partial x_n} \end{array} \right]_{\mathbf{x}=\mathbf{x}^*} \quad (\text{B.4})$$

Then, $\Delta \mathbf{y}$ and $\Delta \mathbf{y}_i$ are eliminated from (B.1) to obtain a simplified form:

$$\begin{aligned}\Delta \dot{\mathbf{x}} &= \tilde{\mathbf{A}}\Delta \mathbf{x} - \tilde{\mathbf{B}}\tilde{\mathbf{D}}^{-1}(\tilde{\mathbf{C}}\Delta \mathbf{x} + \tilde{\mathbf{E}}\Delta u) + \sum_{i=1}^2 \left(\tilde{\mathbf{A}}_i\Delta \mathbf{x}_{\tau_i} - \tilde{\mathbf{B}}_i\tilde{\mathbf{D}}_i^{-1}(\tilde{\mathbf{C}}_i\Delta \mathbf{x}_{\tau_i} + \tilde{\mathbf{E}}_i\Delta u_{\tau_i}) \right) \\ &= \mathbf{A}\Delta \mathbf{x} + \sum_{i=1}^2 \mathbf{A}_i\Delta \mathbf{x}_{\tau_i} + \mathbf{E}\Delta u + \sum_{i=1}^2 \mathbf{E}_i\Delta u_{\tau_i}\end{aligned}\tag{B.5}$$

where \mathbf{A} , \mathbf{E} are the reduced-order Jacobian matrices and \mathbf{A}_i , \mathbf{E}_i are the reduced-order Jacobian matrices with delay:

$$\mathbf{A} = \tilde{\mathbf{A}} - \tilde{\mathbf{B}}\tilde{\mathbf{D}}^{-1}\tilde{\mathbf{C}}\tag{B.6}$$

$$\mathbf{A}_i = \tilde{\mathbf{A}}_i - \tilde{\mathbf{B}}_i\tilde{\mathbf{D}}_i^{-1}\tilde{\mathbf{C}}_i\tag{B.7}$$

$$\mathbf{E} = -\tilde{\mathbf{B}}\tilde{\mathbf{D}}^{-1}\tilde{\mathbf{E}}\tag{B.8}$$

$$\mathbf{E}_i = -\tilde{\mathbf{B}}_i\tilde{\mathbf{D}}_i^{-1}\tilde{\mathbf{E}}_i.\tag{B.9}$$

The linear model (B.5) is transferred into the frequency domain by Laplace transform to get (6).

Appendix C. Parameters for the thermal dynamic model

Thermally related parameters for the 5 m³/hr alkaline electrolysis systems are shown in Table C.4, and the parameters for the cell's U-I curve (A.2) are shown in Table C.5.

References

- [1] IRENA (2020), Green Hydrogen Cost Reduction: Scaling up Electrolyzers to Meet the 1.5°C Climate Goal, International Renewable Energy Agency, Abu Dhabi.
- [2] Brauns, J., Turek, T., 2020. Alkaline Water Electrolysis Powered by Renewable Energy: A Review. *Processes* 8, 248. <https://doi.org/10.3390/pr8020248>
- [3] Hammoudi, M., Henao, C., Agbossou, K., Dubé, Y., Doumbia, M.L., 2012. New multi-physics approach for modelling and design of alkaline electrolyzers. *International Journal of Hydrogen Energy* 37, 13895–13913. <https://doi.org/10.1016/j.ijhydene.2012.07.015>

Table C.4: Parameters for the alkaline electrolysis systems

Parameters	5 Nm ³ /hr
Cell number N_{cell}	26 (13 cells in series)
Cell diameter	0.5 m
Cell area A_{cell}	0.196 m ²
Stack diameter φ_{stack}	0.61 m
Stack length L_{stack}	0.267 m
Stack surface area A_{stack}	1.1 m ²
Electrode volume $V_{\text{stack,electrode}}$	0.03 m ³
Free stack volume $V_{\text{stack,free}}$	0.05 m ³
Stack void fraction at rated f_v	0.5
Blackness of the stack surface $\varepsilon_{\text{stack}}$	0.8
Separator diameter φ_{sep}	0.219 m
Separator length L_{sep}	2 m
Separator volume V_{sep}	1.38 m ³
Separator liquid level $h_{l,\text{sep}}$	50%
Heat transfer coefficient of the cooling coil kA	140 W/K
Lye composition	KOH
Mass fraction of KOH in electrolyte w_{lye}	31.2%
Electrolyte flow rate v_{lye}	0.4-0.6 m ³ /hr
Thermal resistance R_{sep}	0.04 K/W
Stack heat capacity C_{stack}	120 KJ/K
Separator heat capacity C_{sep}	146 KJ/K
Cooling coil heat capacity C_c	23 KJ/K
Stack time-delay τ_1	6 min
Cooling coil time-delay τ_2	4 min

Table C.5: U-I curve parameters

Parameters	Values
r_1	$1.71 \times 10^{-4} \Omega\text{m}^2$
r_2	$-1.96 \times 10^{-7} \Omega\text{m}^2/\text{K}$
s	0.16 V
t_1	$-0.24 \text{ m}^2/\text{A}$
t_2	$26.23 \text{ m}^2\text{K}/\text{A}$
t_3	$139.88 \text{ m}^2\text{K}^2/\text{A}$

- [4] Brauns, J., Turek, T., 2021. Experimental Evaluation of Dynamic Operating Concepts for Alkaline Water Electrolyzers Powered by Renewable Energy. *Electrochimica Acta* 139715. <https://doi.org/10.1016/j.electacta.2021.139715>
- [5] Caparrós Mancera, J.J., Segura Manzano, F., Andújar, J.M., Vivas, F.J., Calderón, A.J., 2020. An Optimized Balance of Plant for a Medium-Size PEM Electrolyzer: Design, Control and Physical Implementation. *Electronics* 9, 871. <https://doi.org/10.3390/electronics9050871>
- [6] Sakas, G., Ibáñez-Rioja, A., Ruuskanen, V., Kosonen, A., Ahola, J., Bergmann, O., 2022. Dynamic energy and mass balance model for an industrial alkaline water electrolyzer plant process. *International Journal of Hydrogen Energy* 47, 4328–4345. <https://doi.org/10.1016/j.ijhydene.2021.11.126>
- [7] Dutton, A., 2000. Experience in the design, sizing, economics, and implementation of autonomous wind-powered hydrogen production systems. *International Journal of Hydrogen Energy* 25, 705–722. [https://doi.org/10.1016/S0360-3199\(99\)00098-1](https://doi.org/10.1016/S0360-3199(99)00098-1)
- [8] Ren, Z., Wang, J., Yu, Z., Zhang, C., Gao, S., Wang, P., 2022. Experimental studies and modeling of a 250-kW alkaline water electrolyzer for hydrogen production. *Journal of Power Sources* 544, 231886. <https://doi.org/10.1016/j.jpowsour.2022.231886>
- [9] Ulleberg, O., 2003. Modeling of advanced alkaline electrolyzers: a system simulation approach. *International Journal of Hydrogen Energy* 28, 21–33. [https://doi.org/10.1016/S0360-3199\(02\)00033-2](https://doi.org/10.1016/S0360-3199(02)00033-2)
- [10] Kojima, H., Matsuda, T., Matsumoto, H., Tsujimura, T., 2018. Development of dynamic simulator of alkaline water electrolyzer for optimizing renewable energy systems. *Journal of International Council on Electrical Engineering* 8, 19–24. <https://doi.org/10.1080/22348972.2018.1436931>
- [11] Dieguez, P., Ursua, A., Sanchis, P., Sopena, C., Guelbenzu, E., Gandia, L., 2008. Thermal performance of a commercial alkaline water electrolyzer: Experimental study and mathematical modeling. *International Journal of Hydrogen Energy* 33, 7338–7354. <https://doi.org/10.1016/j.ijhydene.2008.09.051>

- [12] Busquet, S., Hubert, C.E., Labbé, J., Mayer, D., Metkemeijer, R., 2004. A new approach to empirical electrical modelling of a fuel cell, an electrolyser or a regenerative fuel cell. *Journal of Power Sources* 134, 41–48. <https://doi.org/10.1016/j.jpowsour.2004.02.018>
- [13] Olivier, P., Bourasseau, C., Bouamama, Pr.B., 2017. Low-temperature electrolysis system modelling: A review. *Renewable and Sustainable Energy Reviews* 78, 280–300. <https://doi.org/10.1016/j.rser.2017.03.099>
- [14] Zheng, Y., You, S., Bindner, H.W., Münster, M., 2022. Optimal day-ahead dispatch of an alkaline electrolyser system concerning thermal–electric properties and state-transitional dynamics. *Applied Energy* 307, 118091. <https://doi.org/10.1016/j.apenergy.2021.118091>
- [15] Y. Qiu, B.Zhou, T.Zang, Y.Zhou, R.Qi, J.Lin, Extended load flexibility of industrial P2H plants: A process constraint-aware scheduling approach, in: 2022 IEEE 5th Int. Electrical Energy Conf., Nanjing, China, 2022, pp. 1-6.
- [16] X. Qiu, H.Zhang, Y.Qiu, B.Zhou, T.Zang, R.Qi, J.Lin, J.Wang, Online dynamic parameter estimation of an alkaline electrolysis system based on Bayesian inference, in: 2022 IEEE 5th Int. Electrical Energy Conf., Nanjing, China, 2022, pp. 1-6.
- [17] Rizwan, M., Alstad, V., Jäschke, J., 2021. Design considerations for industrial water electrolyzer plants. *International Journal of Hydrogen Energy* 46, 37120–37136. <https://doi.org/10.1016/j.ijhydene.2021.09.018>
- [18] Qi R, Li J, Lin J, et al. Thermal Modelling and Controller Design of an Alkaline Electrolysis System under Dynamic Operating Conditions[J]. arXiv preprint arXiv:2202.13422, 2022.
- [19] Hernández-Guzmán, Victor Manuel, and Ramón Silva-Ortigoza. Automatic control with experiments. Cham, Switzerland: Springer, 2019.
- [20] Wind integration national dataset toolkit d grid modernization d NREL [WWW Document], n.d, <https://www.nrel.gov/grid/wind-toolkit.html>. [Accessed 7 January 2020].